Earth and Planetary Science Letters 595 (2022) 117764

Contents lists available at ScienceDirect

Earth and Planetary Science Letters

www.elsevier.com/locate/epsl

Transverse aeolian ridges in the landing area of the Tianwen-1 Zhurong rover on Utopia Planitia, Mars

Sheng Gou [a,b,c], Zongyu Yue [a,d], Kaichang Di [a,d,*], Chenxu Zhao [a,e], Roberto Bugiolacchi [b,c,f], Jing Xiao [b,c], Zhanchuan Cai [b,c], Shuanggen Jin [g]

[a] State Key Laboratory of Remote Sensing Science, Aerospace Information Research Institute, Chinese Academy of Sciences, Beijing, China
[b] State Key Laboratory of Lunar and Planetary Sciences, Macau University of Science and Technology, Macau, China
[c] Macau Center for Space Exploration and Science, China National Space Administration, Macau, China
[d] Center for Excellence in Comparative Planetology, Chinese Academy of Sciences, Hefei, China
[e] School of Civil Engineering, Chongqing University, Chongqing, China
[f] Earth Sciences, University College London, London, UK
[g] Shanghai Astronomical Observatory, Chinese Academy of Sciences, Shanghai, China

ARTICLE INFO

Article history:
Received 30 January 2022
Received in revised form 30 July 2022
Accepted 2 August 2022
Available online xxxx
Editor: W.B. McKinnon

Keywords:
Zhurong rover
Utopia Planitia
transverse aeolian ridges
megaripples
Late Amazonian

ABSTRACT

The enigmatic transverse aeolian ridges (TARs), with distinct morphology and albedo, are among the key geological features investigated by China's Tianwen-1 Zhurong rover on southern Utopia Planitia, Mars. Their morphologies and morphometrics are investigated through high-resolution imaging science experiment (HiRISE) orthoimage and Digital Terrain Model (DTM) products. A total of 5089 TARs are identified, with barchan TARs being predominant (97.6%). Morphometric analysis shows these TARs to be small and symmetrical aeolian landforms, with an average crest–ridge lengths of 33.9 ± 20.5 m, profile widths of 9.4 ± 3.8 m, profile heights of 0.4 ± 0.4 m, profile-height-width ratios of 0.04 ± 0.02, and profile symmetry ratios of −0.01 ± 0.13. In-situ observations from the Navigation and Terrain Camera (NaTeCam) show the crests of the TARs to be dark and sharp, while the flanks are interlaced by dark and bright materials. Close-up Multispectral Camera (MSCam) images reveal the TARs to be coated by granules of ∼1.5 mm in diameter. Given the morphometric characteristics and the presence of coating granules, the TARs in the landing area could be categorized as megaripples. Buffered crater counting (BCC) technique-derived absolute model age (AMA) reveals the formation time, or the last active period of the TARs, could be as recent as 1 Ma in the Late Amazonian. The morphometrics and direction of the horns of the barchan TARs suggest the winds for the formation of TARs blew mostly from the north. During the spring-summer transition period (Ls: 50°–93°), the Mars Climate Station (MCS) had recorded local bimodal winds in the landing area, with the speed of the northerly wind in the afternoon being a little stronger than the speed of the southerly wind in the morning. These observations are consistent with the wind fields described in the Mars Climate Database (MCD), which imply the northerly winds during the northern winter season to be responsible for the net sediment transport to the south. Two TARs observed in-situ with secondary NW-SE trending crest-ridges indicate that forked TARs might form given sufficient time (i.e., in the order of millions of years) under modern wind conditions, i.e., the TARs may be currently reworked, if only extremely weakly.

1. Introduction

Tianwen-1, composed of an orbiter, a lander, and a rover named Zhurong, is China's first independent interplanetary mission (Li et al., 2021). On May 15, 2021, the landing platform successfully touched down on Utopia Planitia (Fig. 1a), the largest recognized Martian impact basin with a diameter of 3560 km. The solar powered, six-wheeled Zhurong rover drove off the landing platform on May 21 and is still operating well on the Martian surface at time of writing. The rover has been journeying southwards while investigating rocks, regolith, and other features with its scientific payloads (Fig. 1b).

Aeolian activity is the dominant active geological process at non-polar latitudes on Mars today (Diniega et al., 2021). As wind blows across the Martian surface, it erodes (e.g., through deflation and abrasion) and transport (e.g., through suspension, saltation,

* Corresponding author at: P.O. Box 9718, No. 20A, Datun Road, Chaoyang District, Beijing, 100101, China.
E-mail address: dikc@radi.ac.cn (K. Di).

https://doi.org/10.1016/j.epsl.2022.117764
0012-821X/

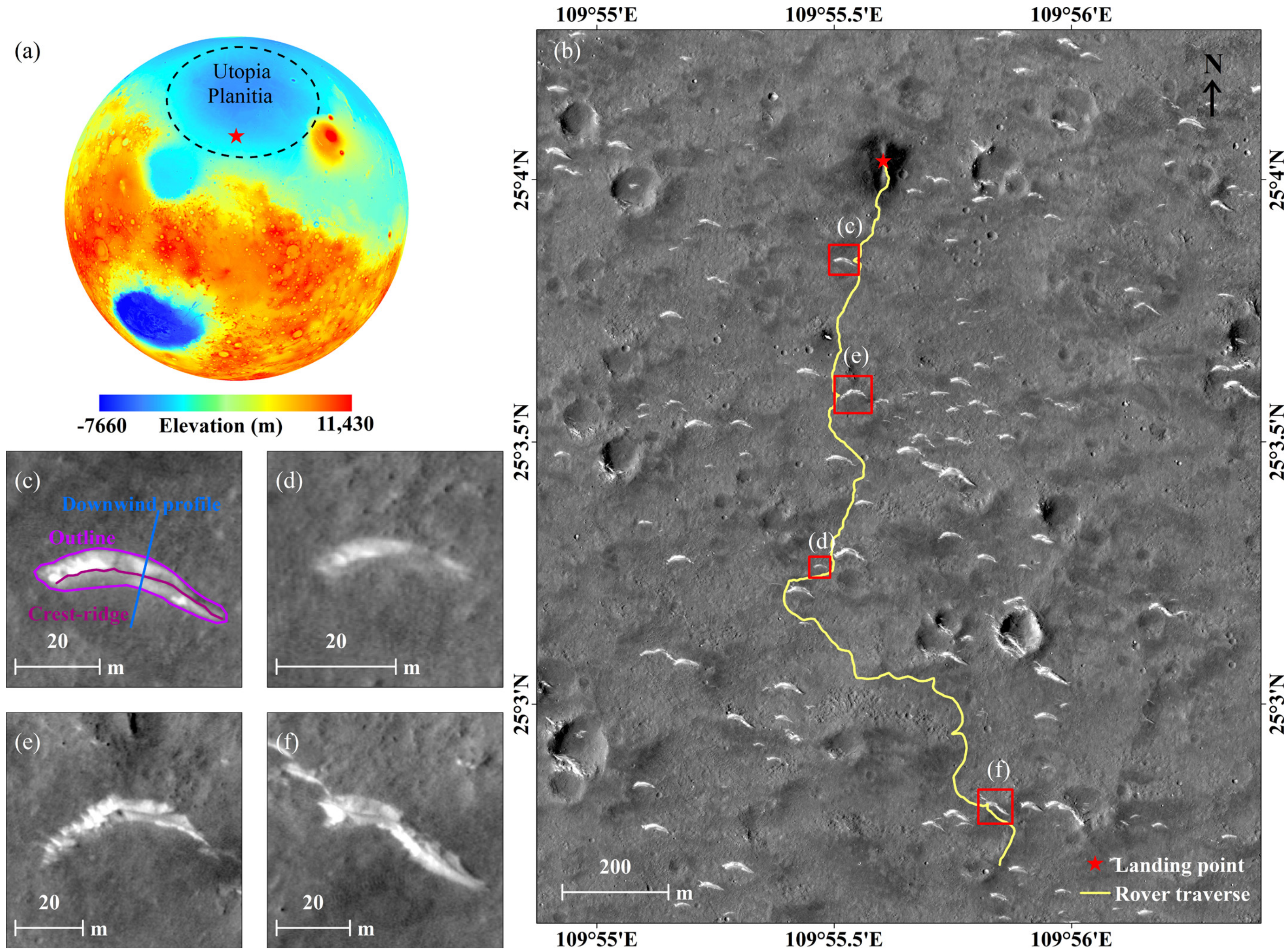

Fig. 1. Context of the landing area of the Tianwen-1 Zhurong rover. (a) Location of the landing point of the Zhurong rover (marked by the red star) within Utopia Planitia. The basemap is a color-coded Mars Orbiter Laser Altimeter (MOLA) topographic map (Smith et al., 2001), with red, green and blue representing high, medium, and low elevations, respectively. The approximate boundary of the Utopia Planitia is outlined by the black dashed circle; (b) Traverse map of the Zhurong rover as of May 15, 2022; (c-f) Examples of TARs observed by the Zhurong rover. Panoramas acquired by the rover for (c) and (d) are shown in Fig. 7 and for (e) and (f) in Fig. 9. (For interpretation of the colors in the figure(s), the reader is referred to the web version of this article.)

and surface creep) regolith particles, and re-organize them into diverse bedforms. Transverse aeolian ridges (TARs) display distinct morphology and albedo, and are the most prominent landforms in the Zhurong landing area. They occur within craters and troughs, around pitted cones, as well as in between these features (Zhao et al., 2021). The term TARs was proposed by Bourke et al. (2003) to describe aeolian landforms that are widely scattered on Mars, but whose age, composition, and origin (e.g., impact ripples, drag ripples, megaripples, reversing dunes, traverse dunes, and dust deposits that were subsequently indurated and eroded) (e.g., Geissler, 2014; Lapotre et al., 2016; Silvestro et al., 2016; Vaz et al., 2017; Lapotre et al., 2018) remain unclear. Previous landed missions (e.g., Opportunity, Spirit, and Curiosity) have investigated the composition, morphology, and dynamics of impact ripples, dark-toned large ripples (DTRs), megaripples, and dunes, few TARs have been studied in detail from the ground (e.g., Sullivan et al., 2005, 2014; Lapotre et al., 2016; Zimbelman and Foroutan, 2020).

Global-scale investigations showed that some TARs might be sourced from locally derived deposits and mostly distributed at low to mid-latitudes in the northern and southern hemispheres within all types of geological settings, irrespective of the regional thermal inertia, elevation, and km-scale roughness (Berman et al., 2011; Geissler, 2014; Berman et al., 2018). With the arrival of high-resolution images, such as those from the high-resolution imaging science experiment (HiRISE) (McEwen et al., 2007), morphometric parameters of the TARs, e.g., width, height, and slope of the profile, crest-ridge length, and wavelength (ridge-to-ridge spacing) were measured and compared with terrestrial analogues (Zimbelman, 2010; Hugenholtz and Barchyn, 2017; Berman et al., 2018; Foroutan and Zimbelman, 2020). TARs have intermediate morphometric characteristics between those of large ripples and dunes, such as meter-scale heights, and decameter-scale wavelengths (Geissler and Wilgus, 2017). Their downwind profiles are normally symmetrical, with the overall average surface slopes $\leq 28°$ and height to wavelength ratios of 0.13–0.15 (Zimbelman, 2010; Balme et al., 2018).

Megaripples (armored with coarse particles) (Wilson and Zimbelman, 2004; Balme et al., 2008; Zimbelman, 2010) and reversing dunes (Zimbelman et al., 2012; Zimbelman and Scheidt, 2014) are proposed as terrestrial analogues for MartianTARs. After detailed morphological and contextual studies on the megaripples in the Puna of Argentina (de Silva et al., 2013), in the Lut Desert of Iran (Hugenholtz and Barchyn, 2017), and in the Sahara Desert of Libya (Foroutan et al., 2019), megaripples are generally considered as the closest terrestrial analogues. TARs are largely thought to be currently inactive, e.g., those investigated by Berman et al. (2018) are thought to have been inactive for 2 million years. However, Silvestro et al. (2020) found evidence of the migration of relatively bright-toned megaripples with 5 m average crest to crest spacing trailing dark sand dunes from repeat HiRISE imagery in high sand flux areas on Mars. Day (2021) further supports the idea that TARs are forward migrating, most similar to the migration of megaripples and dunes. Because TARs are either inactive/immobile or migrating slowly today (Berman et al., 2018; Silvestro et al., 2020; Day, 2021), studying the formation processes of TARs from orbital imagery has not been possible to date. However, if they were inactive/immobile today, TARs could be the key to decipher the recent aeolian activities/landforms on Mars. The Zhurong rover just landed near a sparse field of TARs in the southern Utopia Planitia (Fig. 1b) and carried out in-situ investigations on them, providing a unique opportunity to study these enigmatic features.

2. Data

2.1. HiRISE products

To aid interpretation and morphometric analyses of TARs, we utilized HiRISE (McEwen et al., 2007) stereo image-derived high-resolution Digital Terrain Model (DTM) (grid spacing: 1 m/pixel, vertical accuracy: ∼0.2 m), and the accompanied orthorectified image (spatial resolution: 0.25 m/pixel) (Supplementary Fig. 1). The HiRISE DTM and orthoimage products were downloaded from https://www.uahirise.org/dtm/dtm.php?ID=ESP_069665_2055.

2.2. In-situ measured datasets

As of May 15, 2022, the Zhurong rover had traveled across the Martian surface for one Earth year (Fig. 1b). The datasets from the onboard Navigation and Terrain Camera (NaTeCam), Multispectral Camera (MSCam), and Mars Climate Station (MCS) are used to study the context, geomorphology, and formation of the TARs. The installation positions of the rover's scientific payloads are shown in Supplementary Fig. 2.

The NaTeCam is a color imaging system that is composed of two cameras with identical functions and performance (Li et al., 2021). Each camera has a field of view (FOV) of 46.5° × 46.5°, and acquires images (2,048 × 2,048 pixels) in the visible spectral range of around 400–700 nm (Li et al., 2021). The stereo images are employed to support surface feature analysis, science target designation, topographic mapping, rover localization, rover path planning and navigation, etc. (Li et al., 2021).

The MSCam is a high-resolution multispectral imaging camera with a pixel size of 5.5 μm in the visible and near-infrared bands (Li et al., 2021). Aiming to investigate the morphological characteristics and mineralogic properties of the Martian surface, the MSCam image has a FOV of 24° and a dimension of 2,048 × 2,048 pixels (Li et al., 2021) in panchromatic and multispectral bands (481.3, 526.4, 650.6, 699.2, 800.0, 902.0, 954.0, 1003.0 nm).

The MCS features a temperature sensor, a wind sensor, a pressure sensor, and a microphone (Li et al., 2021) to record a range of meteorological variables, such as temperature, pressure, wind speed and direction. Along with the NaTeCam, the wind sensor and the microphone are mounted on the rover mast (1.8 m above the ground). The sampling rate of the wind sensor is 1 Hz (Li et al., 2021). The measurement range of wind speed is 0-70 m/s, with a resolution of better than 0.5 m/s, and the range of wind direction is 0-360°, with a resolution of 5° (Li et al., 2021).

3. Methods

3.1. Morphometric analyses

Based on the HiRISE orthoimage and DTM products, each TAR is first digitized manually on the ArcGIS® platform, with the crest-ridge being digitized as a polyline and the bedform outline as a polygon. The downwind direction is then inferred based on the curvature of each bedform and the downwind profile is drawn perpendicular to the crest-ridge of the TAR at the midpoint for further analysis. The attributes and morphometrics of each TAR are shown in Fig. 2, and their definitions or calculations (accomplished using python) are described in the text. Note that the ridge-to-ridge spacing (also known as wavelength) is not measured in this study due to the sparse spatial distribution of the TARs (Fig. 1b).

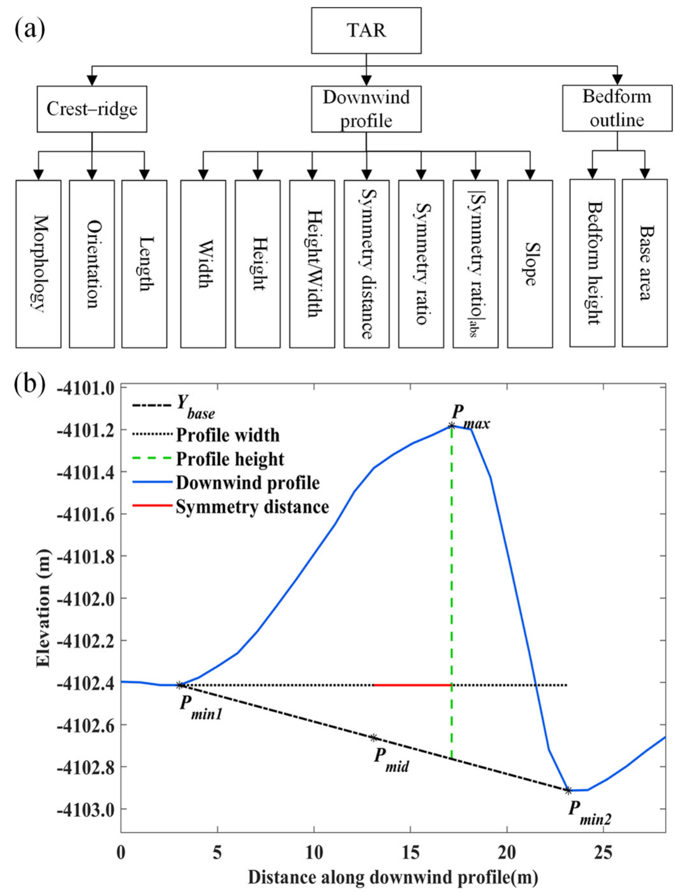

Fig. 2. (a) Attributes and morphometrics of each TAR; (b) Illustration of morphometric analysis on a TAR's downwind profile, which is extracted from Fig. 1c.

Following the first-order classification scheme from Balme et al. (2008), each mapped TAR was assigned one of the following qualitative morphological attribute based on its crest-ridge plan view morphology: 'simple', 'barchan', 'sinuous', 'forked', and 'networked'. The orientation of each TAR was calculated by the "Linear Directional Mean" tool in the ArcGIS®, which outputs the compass angle. The crest–ridge length is defined as the linear extent of the crest–ridge (Fig. 1c).

To calculate parameters related to the downwind profile (Fig. 2b), the highest point of the downwind profile was labeled as P_{max}, the lowest points on either side of the profile were labeled as P_{min1} and P_{min2}, and a line (i.e., Y_{base} in Fig. 2b) that connected the two lowest points was defined using the point-slope formula to represent the basal slope (Berman et al., 2018). The profile width (or downwind length) was defined as the difference in the X values of P_{min1} and P_{min2}. The profile height was defined as the difference in the Y values of P_{max} and Y_{base} at the X value of the P_{max}. The profile symmetry distance is the difference in the X values of P_{max} and the midpoint of P_{min1} and P_{min2} (i.e., P_{mid} in Fig. 2b). A positive value indicates the highest point of the downwind profile is biased to the windward side (i.e., north in this study), where

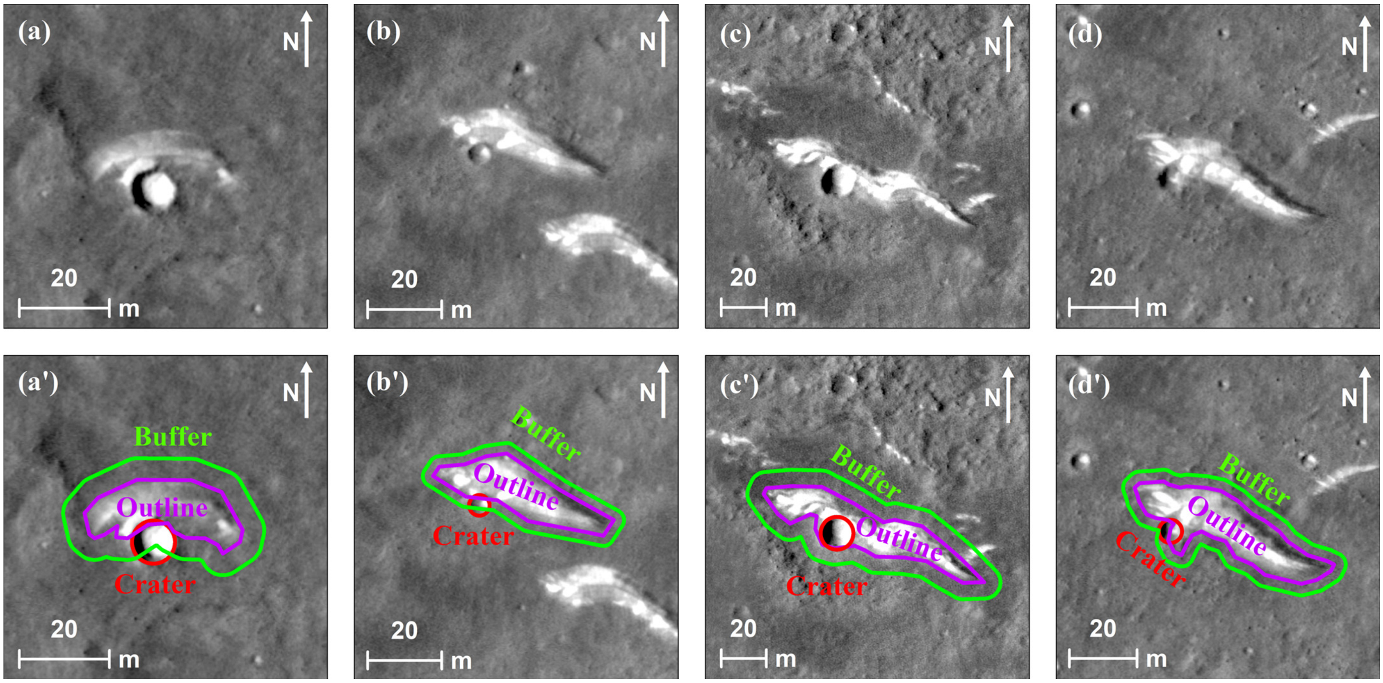

Fig. 3. Examples of craters superposed the TARs. Top panel shows the uninterpreted images (a-d), and the bottom panel images (a'-d') show the outline of TAR, the buffer zone, and the superposed craters in violet, green, and red polygons, respectively. The centers of the sub-figures are (109.897°E, 25.002°N), (109.94°E, 25.008°N), (109.957°E, 25.093°N), and (109.947°E, 25.09°N), respectively.

a negative value suggests the highest point is biased to the leeward side (i.e., south in this study). The profile symmetry ratio represents the ratio between the symmetry distance and the profile width (Berman et al., 2018), and the $|\text{symmetry ratio}|_{abs}$ is the absolute value of the symmetry ratio. The profile slope is calculated by taking the arctangent of twice the height divided by the profile width (Berman et al., 2018).

The landing area of the Zhurong rover is low sloping (average slope is 0.4° at a baseline of 200 m), the basal slope is thus not considered in this study. The bedform height of each TAR is defined as the difference between the highest elevation (H_{max}) within the outline and the mean elevation of the outline (H_{mean}). The base area (or flat surface area) refers to the ground extent of the TAR. The bedform height measured from the outline of a TAR may differ from the profile height when the tallest point on the bedform is located away from measured downwind profile.

3.2. Formation age estimation

During the digitization of the TARs, it was noted that a few small craters in the diameter range of 3-20 m partially superpose the TARs (Fig. 3), indicating that the TARs have probably been inactive under the current climate conditions (or active but extremely slowly). Assuming the TARs in the landing area share a common formation history and considering them as near-linear features, the buffered crater counting (BCC) technique (Kneissl et al., 2015) was employed in this study to determine the absolute model age (AMA) of the TARs, aiming to constrain the formation ages or last active phases of the TARs in the Zhurong landing area.

No ejecta was observed around craters that superposed the TARs, which might be attributed to reworking by active aeolian processes. Therefore, during the implementation of the BCC approach, the applied buffer zone around each TAR was restricted to a width of one crater radius. The creation of the buffer polygons around the TARs and the counting of the craters were carried out using the 'CraterTools' add-on in ArcGIS®, which minimizes distortions raising from map projection (Kneissl et al., 2011). Following a random analysis of the craters, the AMA of the TARs was determined using the Poisson timing analysis with the 'Hartmann and Daubar, 2017' chronology system (Hartmann and Daubar, 2017) available within the 'CraterStats' software (Michael and Neukum, 2010).

The challenge when using the BCC approach to estimate when the TARs formed or were active is that they are geologically very young, and thus the spatially limited counting areas contain only a few craters of any size, let alone hosting craters large enough (e.g., 10 pixels across) to be resolved (Berman et al., 2011). Indeed, only craters >2.5 m in diameter can be reliably mapped based on the HiRISE image. Therefore, only 74 craters were counted within a total surface area of just 1.9 km^2. In addition, due to the unconsolidated nature of the aeolian sediments making up the TARs, the crater diffusion rate might be accelerated, such that the inferred crater-retention ages can only provide a lower limit on the actual age of the TARs.

4. Results and discussions

4.1. Morphometry of TARs

A total of 5089 TARs were identified (Supplementary Fig. 3), covering an area of 1.9 km^2, or 2% of the entire HiRISE image (95.2 km^2). Barchan TARs (97.6%) are predominant in this region, although forked (1.9%) and sinuous (0.5%) are also observed.

Based on observations using HiRISE DTM, it was found that ~40% (2040 out of 5089) of the downwind profiles are not concave down, which is geologically unlikely; consequently, they were excluded from the calculation of profile-related morphometric parameters. Morphometric analyses (Table 1) shows the TARs are small and symmetrical landforms, with crest–ridge lengths of 33.9 ± 20.5 m (expressed in the form of 'mean ± standard deviation'), profile widths of 9.4 ± 3.8 m, profile heights of 0.4 ± 0.4 m, profile symmetry distances of −0.1 ± 1.1 m (i.e., south-facing TAR slopes are slightly steeper than north-facing slopes on average), profile symmetry ratios of −0.01 ± 0.13, profile slopes of 4.5 ±

Table 1
Morphometry of TARs in Zhurong rover landing area.

Attribute		Value					
		Max	Min	Median [25th, 75th percentile]	Mode	Mean	Standard deviation
Crest-ridge[a]	Orientation (°)	148.9	18.2	99.1 [90.9, 105.9]	N/A	98.2	12.0
	Length (m)	384.7	5.1	29.8 [21.2, 41.4]	21.4	33.9	20.5
Downwind profile	Width (m)	37.9	1.8	8.8 [6.9, 10.9]	10.4	9.4	3.8
	Height (m)	3.1	0.1	0.3 [0.2, 0.5]	0.3	0.4	0.4
	Height/Width	0.18	0.00	0.04 [0.02, 0.05]	0.03	0.04	0.02
	Symmetry distance (m)	4.5	−6	0 [−0.94, 0.5]	0	−0.1	1.1
	Symmetry ratio	0.40	−0.39	0 [−0.1, 0.07]	−0.17	−0.01	0.13
	$\lvert$Symmetry ratio$\rvert_{abs}$	0.40	0.00	0.08 [0.05, 0.17]	0.17	0.10	0.08
	Slope (°)	20.7	0.3	4.1 [2.6, 5.9]	2.4	4.5	2.5
Bedform outline	Bedform height (m)	15.8	0.1	0.6 [0.4, 0.9]	0.5	0.7	0.7
	Base area (m^2)	6387.4	33.7	266.5 [164.2, 427.3]	130.7	369.6	+580.4/−369.6

[a] The morphometric parameter values reported for crest-ridge and bedform are from all 5089 TARs, and the values for downwind profile are from the valid 3049 profiles.

2.5°, bedform heights of 0.7 ± 0.7 m, and base areas of 369.6 (+580.4/–369.6) m^2 (the large standard deviation is caused by a few very large areas that skew the values). The box plots and histograms of these parameters are shown in Supplementary Fig. 4. It is noted that many of the parameters measured (e.g., crest-ridge length, downwind profile width, and slope, bedform height and base area) appear to follow log-normal distributions (Supplementary Fig. 4). Accordingly, their modes (i.e., crest-ridge length, downwind profile height/width, bedform base area) shown in Table 1 are calculated from the mean and standard deviation values (Supplementary Text 1).

The mean absolute symmetry ratio and slope of the TARs in the Zhurong landing area (0.1 and 4.5°, respectively) are very similar to the TARs investigated by Berman et al. (2018), who found them with an average symmetry ratio of 0.07, and a profile slope of 6.5°. However, the bedforms of the TARs in other locations on the Martian surface are much larger than those investigated in this work. For example, the average profile width and height of the TARs in Berman et al. (2018) are 24.5 m and 1.5 m, respectively, approximately three times those observed in this study (9.4 m and 0.4 m, respectively). In addition, Hugenholtz et al. (2017) found in their study that a typical TAR has a crest-ridge length of 88.5 m, a profile width and height of 17.3 m and 1.3 m, respectively. When the profile heights are scaled by the profile widths, the ratio values (0.04 ± 0.02) deviate from those measured for reversing dunes and traverse dunes, and appear much closer to the values of terrestrial granule megaripples and pebble-coated megaripples (Zimbelman et al., 2012) (Fig. 4). Day and Zimbelman (2021) suggest the term "megaripple" to be reserved for the morphology when coarse grain content is known or explicitly interpreted from the geologic context. Therefore, the profile height-width ratio values cannot be used as a diagnostic indicator of bedform type, whereas ground observations could.

4.2. Orientations of TARs

The orientations of the crest-ridges TARs in the landing area are regionally consistent. They trend broadly in the east-west direction (98.2 ± 12.0°) (Table 1 and Fig. 5), suggesting they share a common formation history. The numbers of TARs with a positive and negative symmetry distance are 1191 (39%) and 1390 (46%), respectively. The remaining 468 (15%) have zero values, betraying their highly symmetrical morphology. The south-pointing of the horns of the barchan TARs (Fig. 1b) and slightly more negative values (i.e., the highest points are biased to the south) suggest that past regional sediment-transporting winds that formed TARs blew mostly from the north towards the south, and slightly more sediments were transported by the northerly winds, i.e., net sediment flux to the south.

4.3. Absolute model age of TARs

The absolute model age (AMA) derived from the BCC technique for the TARs in the Zhurong landing area is $1.0^{+0.2}_{-0.2}$ Ma (Fig. 6), suggesting that the formation epoch or the last active period of the TARs was in the Late Amazonian. Given the sample size (74 craters), the very small surface area (1.9 km^2), and the very small scale of craters (3–20 m in diameter) considered here, it is worth stressing that determining the model age of these TARs stretches the boundaries of reliability for the crater counting methodology. Even for areas up to 10,000 km^2 and much larger sample populations, Palucis et al. (2020) demonstrated that age uncertainties can overwhelm the signal. When measured over a small range of diameters, crater ages become very sensitive to statistical outliers (Rubanenko et al., 2021). Furthermore, such small impacts tend to occur in clusters (Daubar et al., 2013), yielding a significant challenge to using crater-density statistics over such small counting areas and discriminating between primary and secondary impacts

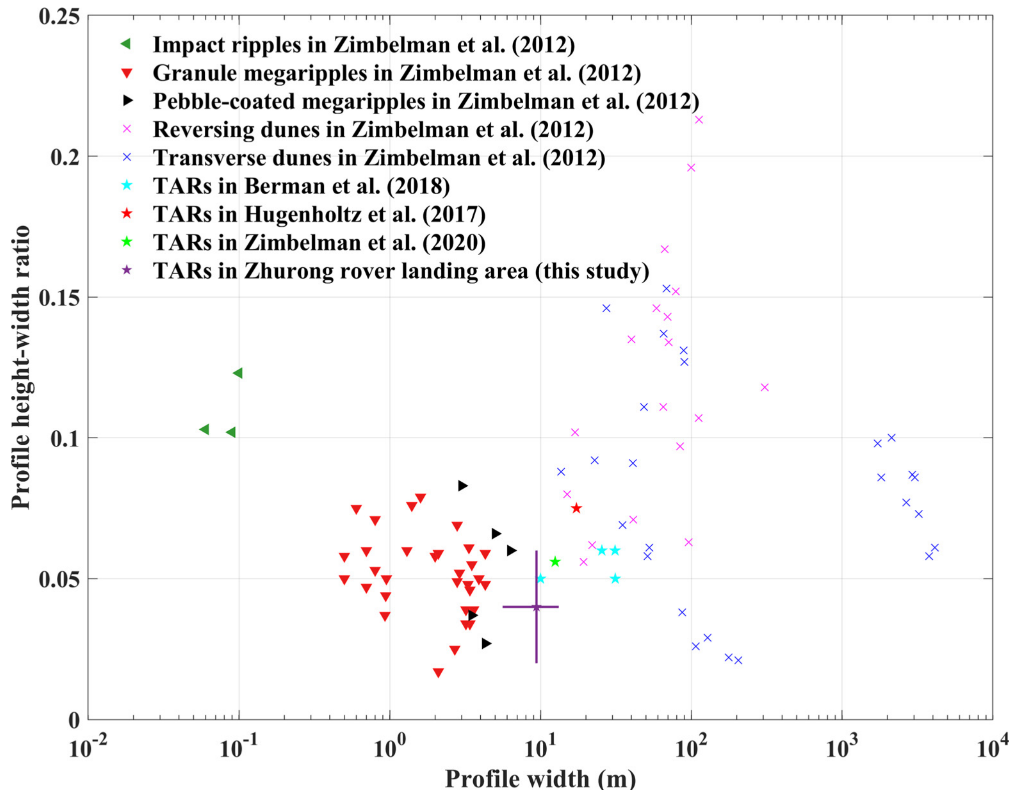

Fig. 4. Scatter plot of downwind profile width versus profile height-width ratio for terrestrial aeolian landforms (i.e., impact ripples, granule megaripples, pebble-coated megaripples, reversing dunes, and transverse dunes) (Zimbelman et al., 2012), previously investigated Martian TARs (Hugenholtz et al., 2017; Berman et al., 2018; Zimbelman and Foroutan, 2020), and TARs in the Zhurong landing area. This figure is modified after Zimbelman et al. (2012) and Berman et al. (2018).

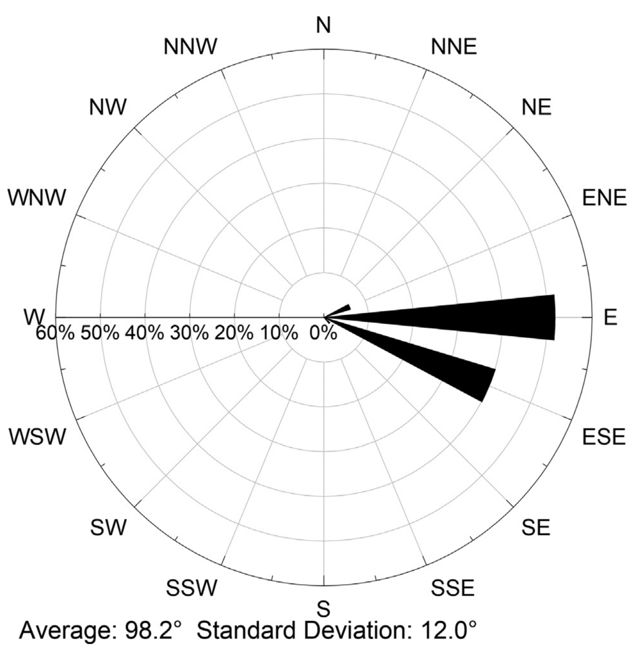

Fig. 5. Orientations of the crest-ridges of the TARs in the Zhurong landing area.

(the latter being clearly redundant). Therefore, the reported model age of 1 Ma should be taken as an indicative estimation and the actual uncertainty probably much larger than that provided by the 'CraterStats' calculation.

The reported 1 Ma model age in this study is very close to that of the TARs or dunes in other Martian regions; for instance, Berman et al. (2011) reported TARs in the equatorial Meridiani region have crater retention ages of ∼1–3 Ma, while those in the southern intra-crater dunefields appear to be no older than ∼100 Ka. Reiss et al. (2004) estimated that the transverse dunes in the valley floor of Nirgal Vallis ceased to be active approximately 1.4–0.3 Ma ago.

4.4. Observations from Zhurong rover and implications

4.4.1. Ground observations of TARs

The Zhurong rover has carried out close-up observations on the TARs (Fig. 7). The panoramas produced from the NaTeCam images show most of their surfaces to be very smooth at a decimeter scale, whereas the surrounding terrain is rough and rocky. It is observed from the panoramas that a small number of rocks are perched on the rugged bedrock surface (Fig. 7a, c), while most are partially buried below the surface. Zhao et al. (2021) derived an AMA of 757 ± 66 Ma for bedrock substrate that dominates the central and eastern parts of the Zhurong landing area. Further, a local resurfacing process in the Amazonian period was proposed due to the large discrepancy between their estimate and the estimated model age of the Vastitas Borealis Formation (VBF) unit (Zhao et al., 2021). These exposed rocks might represent the product of the resurfacing process that occurred 757 ± 66 Ma ago. The superposition relationship between the rocks and the TARs reveals the last activity of the TARs postdates the formation of the underlying bedrock, and thus that the TARs should be younger than 757 ± 66 Ma.

TARs are bright-toned in HiRISE images (Fig. 1c and d); however, ground observations from the NaTeCam (Fig. 7a and g) shows there are visible variations in tone on the surface of the TARs. The sharp crests are usually dark–toned, while the flanks are generally bright with interlaced black materials. MSCam images reveal the ground to be covered with pebbles and cobbles (∼4-50 cm) (Fig. 7c and d) and the dark-toned surfaces are armored by granules (∼1.5

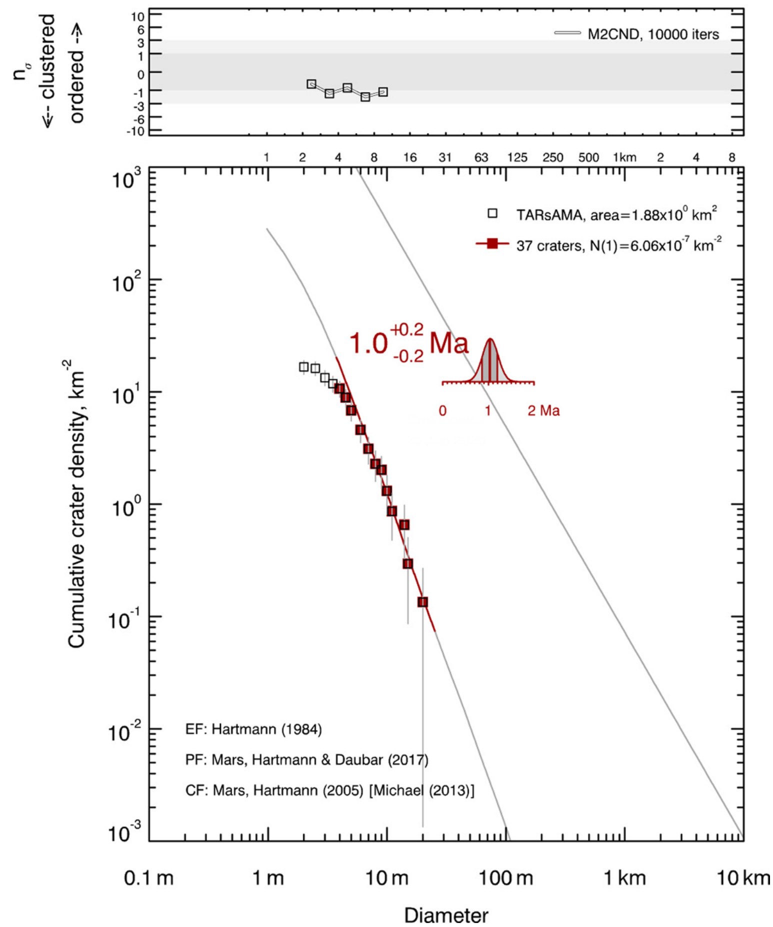

Fig. 6. Averaged AMA of the TARs in the Zhurong rover landing area.

mm in diameter) (Fig. 7e and h). The particle sizes of the light-toned surfaces cannot be resolved at a millimeter scale (Fig. 7f and i). MSCam spectra of these bright-toned materials, dark-toned materials, and granules have similar features (Supplementary Figs. 5), indicating they probably derive from the same source.

Based on the morphometric characteristics and the mantling of granules on the surface, the TARs in the landing area of the Zhurong rover should be categorized as megaripples when the recommendations for Mars' aeolian bedform terminology are adopted (Day and Zimbelman, 2021). In-situ observations from other rovers also suggest that TARs are probably megaripples. For instance, a relatively small TAR traversed by the Curiosity rover at Dingo Gap is thought to be a megaripple due to a mantling of large grains (1–2 mm in diameter, well-rounded particles) that are too massive to be activated by saltation (Zimbelman and Foroutan, 2020; Bretzfelder and Day, 2021). The gravel- or granule-mantled megaripples in the Gusev crater and Meridiani Planum observed by the Mars Exploration Rovers (Spirit and Opportunity) resemble larger nearby TARs, and it was suggested that the TARs might also be granule-mantled megaripples (Sullivan et al., 2005; Jerolmack et al., 2006; Balme et al., 2008; Sullivan et al., 2008, 2014).

4.4.2. Measurements of local winds

Bimodal winds that could have contributed to the symmetrical profile of the bedform of a TAR (Zimbelman and Foroutan, 2020) have been recorded by the MCS onboard Zhurong rover. A southerly prevailing wind in the morning (Fig. 8a) switching to a northerly prevailing wind in the afternoon (Fig. 8b) were observed during the northern spring-summer transition period (L_S: 50°–95°). The average speed of the northerly wind is a little stronger than that of the southerly one (Fig. 8a-b). During the northern summer-autumn transition period (L_S: 119°–149° and 152°–181°), the MCS carried out measurements only in the morning and recorded the wind mostly blowing from the south (Fig. 8c) and southwest (Fig. 8d). A more detailed illustration of wind speed and direction shown at different time intervals can be found in Supplementary Figs. 6–9 and Supplementary Tables 1–3.

According to the Mars Climate Database (MCD) (Lewis et al., 1999), a database of meteorological fields derived from General Circulation Model (GCM) numerical simulations of the Martian atmosphere and validated using available observational data, the local surface wind fields in the Zhurong landing area experience significant seasonal and diurnal fluctuations (Fig. 8e). The strongest wind blows from south in the morning but switches to the north in the afternoon (Fig. 8e) during the northern spring-summer and summer-autumn transitions.

The rover's in-situ MCS measurements are consistent with the wind fields in the MCD, indicating the MCD has been better validated and are more trustworthy. The MCS/MCD agreement increases confidence that the MCD output is a realistic wind field. Thus, the output of the wind fields from the MCD during the Zhurong-unmeasured seasons (e.g., norther winter) is extremely helpful in the context of inferring the formation and evolution of TARs.

Analysis of the orientations of the crest-ridges of TARs shows a predominantly west-east trend (Fig. 5), which suggests that their formation in this region is driven primarily by regional winds. The morphologies of the TARs imply the winds blew mostly from the north (see Section 4.2). The Zhurong rover only measured the

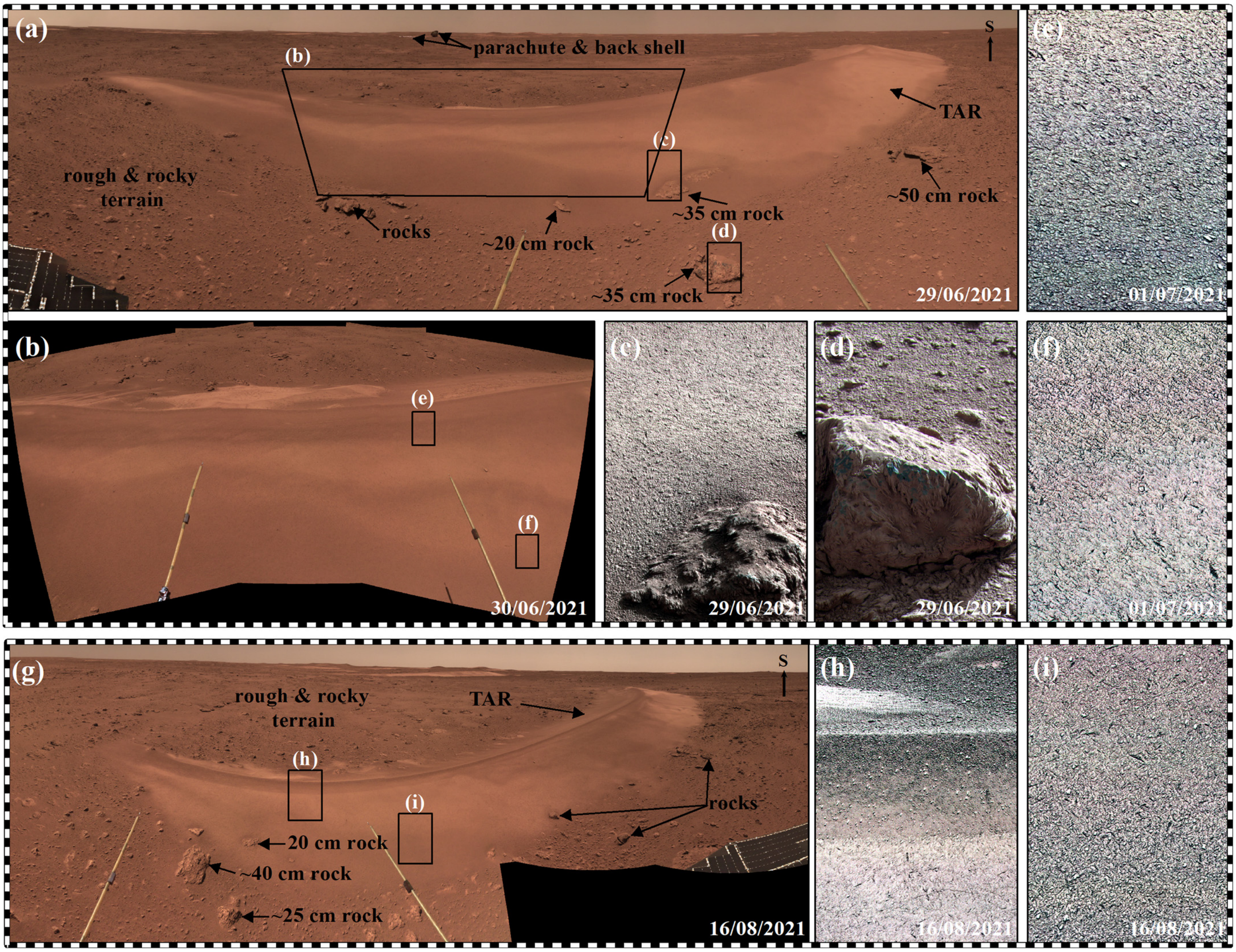

Fig. 7. NaTeCam (a, b, g) panoramas and MSCam color images (red: 650.6 nm, green: 526.4 nm, blue: 481.3 nm) (c, d, e, f, h, i) of two barchan TARs observed by the Zhurong rover. The TAR shown in (a) is ~200 m southwest of the landing point, with a bedform height of ~1.1 m, a downwind profile width of ~8.2 m, and a crest–ridge length of ~43.3 m. The TAR shown in (g) is ~732 m south of the landing point, with a bedform height of ~1.2 m, a downwind profile width of ~12.2 m, and a crest–ridge length of ~67.7 m. HiRISE images of the two TARs are shown in Fig. 1c and d. The MSCam image is ~25 cm across.

wind fields for the northern spring-summer and summer-autumn transitions (Fig. 8a-d), which are Mars' low wind seasons. Previous studies (orbital and ground-based) have demonstrated that little sediment transport occurs outside of the northern winter (dust storm season) (e.g., Ayoub et al., 2014; Bridges et al., 2017; Baker et al., 2018). Consequently, it seems unlikely that the rover measured winds reported here could be responsible for a significant net sediment transport to the south, whereas the Zhurong-unmeasured strong and dominant northern winter northerly winds might (Fig. 8e).

4.4.3. Implications for TARs evolution

The TARs-forming northerly winds as inferred from TARs morphology/morphometry (see Section 4.2) and the modern strong winter northerly winds are similar, indicating the prevailing winds in the landing area have not changed notably since TARs formed and the TARs might be still evolving. It is understood from the morphology that barchan TARs are predominant and forked TARs are rarely observed in this region. According to a study on the multistage evolution of TARs (Nagle-McNaughton and Scuderi, 2021), it is inferred that the TARs in the landing area should survive for a significant time (i.e., in the order of millions of years) before evolving into other morphologies. It means that the TARs might be subjected to erosion under current Martian climate conditions when a secondary crest-ridge morphology that differs from the present barchan TARs develop gradually. NaTeCam panoramas from the rover indeed observed TARs with secondary NW-SE trending crest-ridges are developing as bifurcations (Fig. 9a and d). This implies that forked TARs might form after a long enough time (i.e., in the order of millions of years) under modern climate conditions (especially the strong northerly winds during the winter, Fig. 8e). MSCam images (Fig. 9b and c) also confirm the presence of granules on the surfaces of these secondary TARs.

The sparse spatial distribution and relatively stable bedforms of the TARs in the landing area indicate that the modern winds seem unable to mobilize the TARs. There are three possible scenarios to explain the immobility of the TARs: (i) the modern aeolian activity might have weakened; (ii) the surfaces of the TARs might have been indurated/cemented by salt; (iii) the surfaces of TARs might have been stabilized by dust.

In the first scenario, the developing of secondary NW-SE trending crest-ridges as bifurcations indicates there might be still active saltation of sands on these secondary TAR crests under modern climate conditions, and these aeolian activities cannot mobilize the primary TARs due to the mantling of granules, i.e., the modern winds might have weakened such that particles once mobile

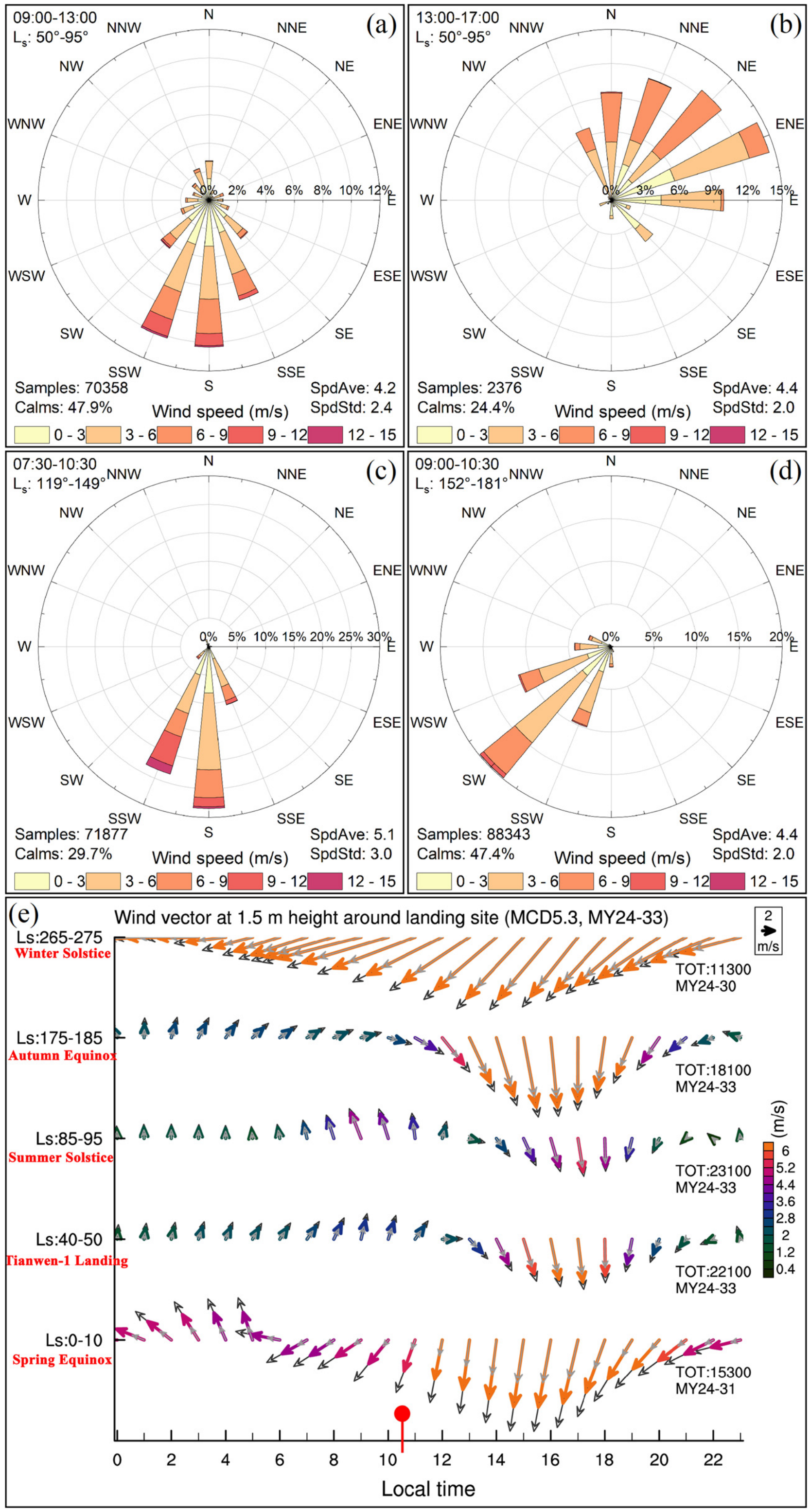

Fig. 8. (a)–(d) Rose charts of in-situ measured near-surface wind speed and direction at different periods. (e) Distribution of surface wind fields in the vicinity of the landing area of the Zhurong rover at different local times for Mars year (MY) 24-33. The colored arrows stand for the mean wind speeds, and the grey arrows represent the mean wind speeds +/− one standard deviation. The red mark between 10:00 and 11:00 on the abscissa indicates the main observation time of the rover during the spring-summer transition period (L_s: 50°–95°).

on the primary TARs have become immobile. During the Zhurong rover's traverse to the south, it has observed there are craters that were/are infilled by aeolian sediments (Supplementary Fig. 10), indicating that much of today's Martian surface is still actively being modified by aeolian activities.

In the second scenario, various geological features in the landing area, including ghost craters, troughs, pitted cones, and layered ejecta craters, indicate the possible presence of volatiles (e.g., water/ice) in the shallow subsurface. The analysis of the in-situ measured spectra reveals there are hydrated sulfate/silica materials

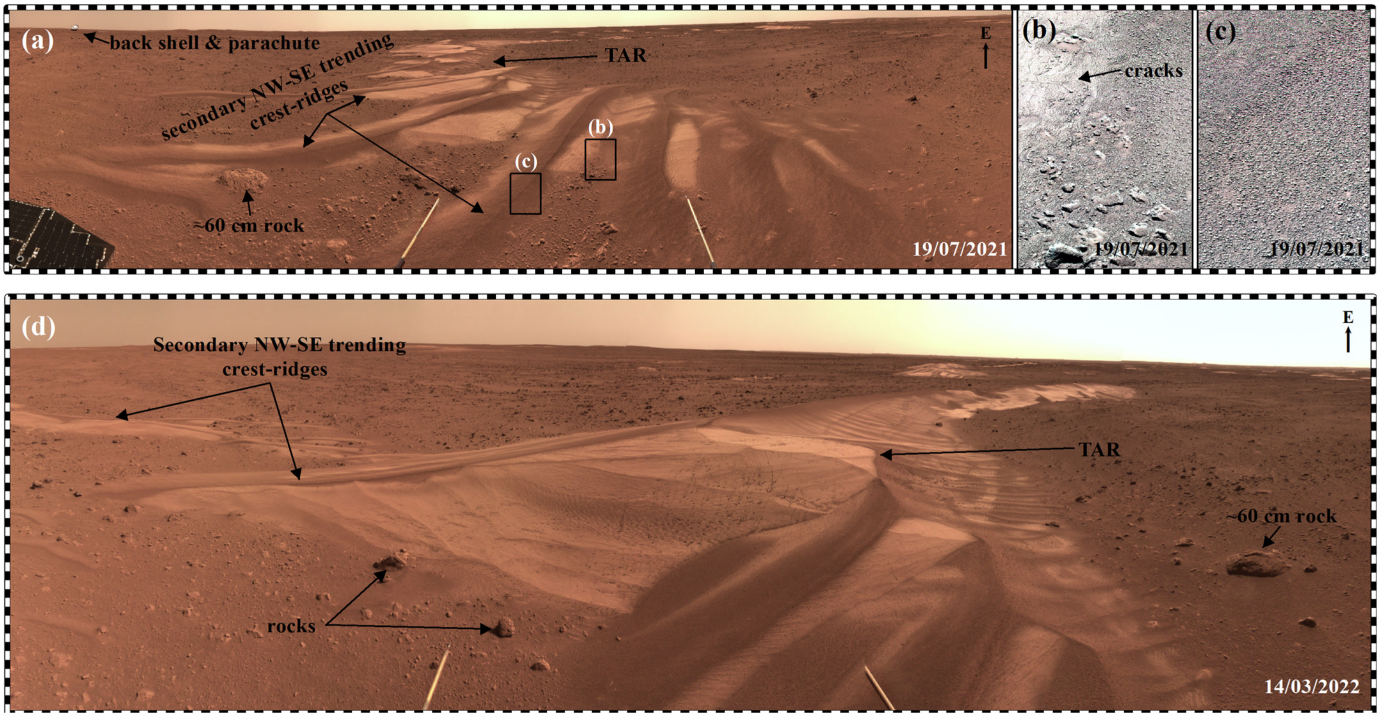

Fig. 9. NaTeCam panoramas (a, d) and MSCam color images (b, c) (red: 650.6 nm, green: 526.4 nm, blue: 481.3 nm) of two TARs with secondary NW-SE trending crest-ridges. The TAR shown in (a) is ~732 m south of the landing point, with a bedform height of ~0.7 m, a downwind profile width of ~8.5 m, and a crest–ridge length of ~58.5 m. The TAR shown in (d) is ~1223 m southeast of the landing point, with a bedform height of ~0.7 m, a downwind profile width of ~8.2 m, and a crest–ridge length of ~54.2 m. HiRISE images of the two TARs are shown in Fig. 1e and f. The MSCam image is ~25 cm across.

on the Amazonian terrain at the Zhurong landing area, indicating a more active Amazonian hydrosphere than previously thought (Liu et al., 2022). In addition, cracks, which occur due to thermal contraction or loss of materials (particularly volatiles), are also observed on the flanks of the TARs (Fig. 9b). Therefore, the surface of the TARs might have been indurated/cemented by those intergranular water-bearing minerals.

In the third scenario, the threshold wind speed required to mobilize dust is much higher than that necessary to transport sand (and in fact, vigorous saltation of sand is thought to be a prerequisite to splash dust into suspension) (Kok et al., 2012). Since landing on Mars, Zhurong rover has been constantly exposed to Martian winds and dust. A thin layer of dust has accumulated on the Zhurong rover, e.g., calibration plate (Supplementary Fig. 11a-b). Dust deposition is a common phenomenon on Mars surface, it was also observed on NASA rovers' calibration plates, e.g., Opportunity and Spirit (Supplementary Fig. 11c-f). Although the MSCam does not directly observe a thin or thick veneer of dust on the surfaces of TARs, the close-up images of the rocks show the top of one rock is covered by a moderately thick dust (Fig. 7c) and the windward face of another rock is full of grooves (Fig. 7d) that probably were shaped by abrasion. These observations reveal that the past aeolian activities were strong and the dust deposition is common in present climate conditions. It's inferred from the dust cover index (DCI) value (<0.94) (Ruff and Christensen, 2002) that the TARs in the landing area might be in a 'heavily dust covered' state. Considering the implication of DCI value and the observed dust deposition on both the calibration plate and rocks, it's proposed that a moderately thick veneer of dust on the surfaces of TARs alone might result in the demise of a previously active bedform.

Since the formation and migration of TARs is not completely understood, the immobility of the primary TARs is probably explained a combination of the above mentioned three scenarios. To validate the immobility of the TARs, a series of high-resolution images, such as multi-temporal HiRISE images, are needed to establish whether the morphology and position of TARs have changed with time.

5. Conclusion

A total of 5089 TARs were identified from a HiRISE orthoimage that covers the landing area of the Zhurong rover, with barchan TARs (97.6%) representing the predominant type. These small and symmetrical TARs are the dominant aeolian landforms in this region, with crest-ridge lengths of 33.9 ± 20.5 m, profile widths of 9.4 ± 3.8 m, profile heights of 0.4 ± 0.4 m, profile symmetry distances of −0.1 ± 1.1, profile symmetry ratios of −0.01 ± 0.13 m, profile slopes of 4.5 ± 2.5°, bedform heights of 0.7 ± 0.7 m, and base areas of 369.6 (+580.4/–369.6) m^2. The profile height-width-ratio values (0.04 ± 0.02) are much closer to those of terrestrial megaripples than to reversing dunes and traverse dunes.

NaTeCam panoramas reveal the sharp crests of TARs to be dark, and the flanks are interlaced bright and dark. MSCam images reveal that the crests are covered by granules of ~1.5 mm in diameter. These in-situ observations and morphometric characteristics suggest that the TARs in the landing area should be categorized as megaripples.

The orientations of the crest-ridges of the TARs show predominantly west-east trends, suggesting they had a common formation history, and their formation was controlled primarily by regional large-scale northerly winds. An approximate model age estimate by the buffered crater counting (BCC) technique reveals the formation epoch, or the last active period of the TARs was during the Late Amazonian, i.e., $1.0^{+0.2}_{-0.2}$ Ma. Given the sample size, the very small surface area, and the very small scale of craters considered here, there is large uncertainty of the reported model age.

Meteorological data measured in-situ reveal bimodal winds in the landing area during the spring-summer transition period (Ls: 50°–95°). The average speed of the northerly wind in the afternoon is a little stronger than that of the southerly wind in the morning. In the morning of the northern summer-autumn transition period (Ls: 119°–149° and 152°–181°), the Zhurong rover observed the wind mostly blowing from the south and the southwest. These observations are consistent with the wind fields from the Mars Climate Database (MCD), suggesting that the winds have not changed notably since TARs formed and that the TARs should be stable for quite a long time before evolving into other morphologies. NaTeCam panoramas of two TARs with secondary NW-SE trending crest-ridges imply that forked TARs might form given enough time (i.e., in the order of millions of years) under modern wind conditions (i.e., the TARs may currently be reworked, if only extremely slowly).

CRediT authorship contribution statement

Sheng Gou: Conceptualization, Data curation, Funding acquisition, Methodology, Writing – original draft, Writing – review & editing. **Zongyu Yue:** Formal analysis, Funding acquisition, Investigation, Writing – original draft, Writing – review & editing. **Kaichang Di:** Conceptualization, Funding acquisition, Investigation, Supervision, Writing – original draft, Writing – review & editing. **Chenxu Zhao:** Data curation, Software, Validation, Writing – original draft, Writing – review & editing. **Roberto Bugiolacchi:** Formal analysis, Funding acquisition, Validation, Writing – review & editing. **Jing Xiao:** Validation, Visualization, Writing – review & editing. **Zhanchuan Cai:** Supervision, Validation, Writing – review & editing. **Shuanggen Jin:** Funding acquisition, Validation, Writing – review & editing.

Declaration of competing interest

The authors declare that they have no known competing financial interests or personal relationships that could have appeared to influence the work reported in this paper.

Data availability

The authors do not have permission to share data.

Acknowledgements

The Tianwen-1 datasets are processed and produced by Ground Research and Application System (GRAS) of China's Lunar and Planetary Exploration Program (CLEP) and are provided by China National Space Administration (CNSA) (https://moon.bao.ac.cn/web/enmanager/home). The authors are also thankful to the HiRISE team for making the DTM and orthoimage of the Tianwen-1 landing area available. This research is supported by the Strategic Priority Research Program of the Chinese Academy of Sciences (Grant No. XDB41000000), National Key Research and Development Program of China (Grant No. 2021YFA0716100), National Natural Science Foundation of China (Grant No. 42172265), and Macao Young Scholars Program (Grant No. AM201902). Constructive reviews by Matt Balme, Mackenzie Day and an anonymous reviewer improved the quality of this manuscript substantially and are greatly appreciated. We also thank William B. McKinnon for the efficient and helpful editorial handling.

Appendix A. Supplementary material

Supplementary material related to this article can be found online at https://doi.org/10.1016/j.epsl.2022.117764.

References

Ayoub, F., Avouac, J.P., Newman, C.E., Richardson, M.I., Lucas, A., Leprince, S., Bridges, N.T., 2014. Threshold for sand mobility on Mars calibrated from seasonal variations of sand flux. Nat. Commun. 5 (1), 5096.

Baker, M.M., Newman, C.E., Lapotre, M.G.A., Sullivan, R., Bridges, N.T., Lewis, K.W., 2018. Coarse sediment transport in the modern Martian environment. J. Geophys. Res., Planets 123 (6), 1380–1394.

Balme, M., Berman, D.C., Bourke, M.C., Zimbelman, J.R., 2008. Transverse Aeolian Ridges (TARs) on Mars. Geomorphology 101 (4), 703–720.

Balme, M., Robson, E., Barnes, R., Butcher, F., Fawdon, P., Huber, B., Ortner, T., Paar, G., Traxler, C., Bridges, J., Gupta, S., Vago, J.L., 2018. Surface-based 3D measurements of small aeolian bedforms on Mars and implications for estimating ExoMars rover traversability hazards. Planet. Space Sci. 153, 39–53.

Berman, D.C., Balme, M.R., Rafkin, S.C.R., Zimbelman, J.R., 2011. Transverse Aeolian Ridges (TARs) on Mars II: distributions, orientations, and ages. Icarus 213 (1), 116–130.

Berman, D.C., Balme, M.R., Michalski, J.R., Clark, S.C., Joseph, E.C.S., 2018. High-resolution investigations of transverse aeolian ridges on Mars. Icarus 312, 247–266.

Bourke, M.C., Wilson, S.A., Zimbelman, J.R., 2003. The variability of transverse aeolian ripples in troughs on Mars. In: 34th Lunar and Planetary Science Conference. League City, Texas, p. 2090.

Bretzfelder, J.M., Day, M., 2021. Alien aeolian bedforms: a comparative sedimentary analysis of the dingo gap bedform and hidden valley ripple traverses, Gale Crater, Mars. J. Geophys. Res., Planets 126 (8), e2021JE006904.

Bridges, N.T., Sullivan, R., Newman, C.E., Navarro, S., van Beek, J., Ewing, R.C., Ayoub, F., Silvestro, S., Gasnault, O., Le Mouélic, S., Lapotre, M.G.A., Rapin, W., 2017. Martian aeolian activity at the Bagnold Dunes, Gale Crater: the view from the surface and orbit. J. Geophys. Res., Planets 122 (10), 2077–2110.

Daubar, I.J., McEwen, A.S., Byrne, S., Kennedy, M.R., Ivanov, B., 2013. The current martian cratering rate. Icarus 225 (1), 506–516.

Day, M., 2021. Interaction bounding surfaces exposed in migrating transverse aeolian ridges on Mars. Geology 49 (12), 1527–1530.

Day, M., Zimbelman, J.R., 2021. Ripples, megaripples, and TARs, Oh, My! Recommendations regarding Mars aeolian bedform terminology. Icarus 369, 114647.

de Silva, S.L., Spagnuolo, M.G., Bridges, N.T., Zimbelman, J.R., 2013. Gravel-mantled megaripples of the Argentinean Puna: a model for their origin and growth with implications for Mars. Geol. Soc. Am. Bull. 125 (11–12), 1912–1929.

Diniega, S., Bramson, A.M., Buratti, B., Buhler, P., Burr, D.M., Chojnacki, M., Conway, S.J., Dundas, C.M., Hansen, C.J., McEwen, A.S., Lapôtre, M.G.A., Levy, J., Mc Keown, L., Piqueux, S., Portyankina, G., Swann, C., Titus, T.N., Widmer, J.M., 2021. Modern Mars' geomorphological activity, driven by wind, frost, and gravity. Geomorphology 380, 107627.

Foroutan, M., Steinmetz, G., Zimbelman, J.R., Duguay, C.R., 2019. Megaripples at Wau-an-Namus, Libya: a new analog for similar features on Mars. Icarus 319, 840–851.

Foroutan, M., Zimbelman, J.R., 2020. Evaluation of large data sets for Transverse Aeolian Ridges (TARs) on Earth and Mars. Planet. Space Sci. 189, 104966.

Geissler, P.E., 2014. The birth and death of transverse aeolian ridges on Mars. J. Geophys. Res., Planets 119 (12), 2583–2599.

Geissler, P.E., Wilgus, J.T., 2017. The morphology of transverse aeolian ridges on Mars. Aeolian Res. 26, 63–71.

Hartmann, W.K., Daubar, I.J., 2017. Martian cratering 11. Utilizing decameter scale crater populations to study Martian history. Meteorit. Planet. Sci. 52 (3), 493–510.

Hugenholtz, C.H., Barchyn, T.E., 2017. A terrestrial analog for transverse aeolian ridges (TARs): environment, morphometry, and recent dynamics. Icarus 289, 239–253.

Hugenholtz, C.H., Barchyn, T.E., Boulding, A., 2017. Morphology of transverse aeolian ridges (TARs) on Mars from a large sample: further evidence of a megaripple origin? Icarus 286, 193–201.

Jerolmack, D.J., Mohrig, D., Grotzinger, J.P., Fike, D.A., Watters, W.A., 2006. Spatial grain size sorting in eolian ripples and estimation of wind conditions on planetary surfaces: application to Meridiani Planum, Mars. J. Geophys. Res., Planets 111. E12.

Kneissl, T., van Gasselt, S., Neukum, G., 2011. Map-projection-independent crater size-frequency determination in GIS environments—new software tool for ArcGIS. Planet. Space Sci. 59 (11), 1243–1254.

Kneissl, T., Michael, G.G., Platz, T., Walter, S.H.G., 2015. Age determination of linear surface features using the Buffered Crater Counting approach – case studies of the Sirenum and Fortuna Fossae graben systems on Mars. Icarus 250, 384–394.

Kok, J.F., Parteli, E.J., Michaels, T.I., Karam, D.B., 2012. The physics of wind-blown sand and dust. Rep. Prog. Phys. 75 (10), 106901.

Lapotre, M.G.A., Ewing, R.C., Lamb, M.P., Fischer, W.W., Grotzinger, J.P., Rubin, D.M., Lewis, K.W., Ballard, M.J., Day, M., Gupta, S., Banham, S.G., Bridges, N.T., Des Marais, D.J., Fraeman, A.A., Grant, J.A., Herkenhoff, K.E., Ming, D.W., Mischna, M.A., Rice, M.S., Sumner, D.Y., Vasavada, A.R., Yingst, R.A., 2016. Large wind ripples on Mars: a record of atmospheric evolution. Science 353 (6294), 55–58.

Lapotre, M.G.A., Ewing, R.C., Weitz, C.M., Lewis, K.W., Lamb, M.P., Ehlmann, B.L., Rubin, D.M., 2018. Morphologic diversity of Martian ripples: implications for large-ripple formation. Geophys. Res. Lett. 45 (19), 10,229–210,239.

Lewis, S.R., Collins, M., Read, P.L., Forget, F., Hourdin, F., Fournier, R., Hourdin, C., Talagrand, O., Huot, J.-P., 1999. A climate database for Mars. J. Geophys. Res., Planets 104 (E10), 24177–24194.

Li, C., Zhang, R., Yu, D., Dong, G., Liu, J., Geng, Y., Sun, Z., Yan, W., Ren, X., Su, Y., Zuo, W., Zhang, T., Cao, J., Fang, G., Yang, J., Shu, R., Lin, Y., Zou, Y., Liu, D., Liu, B., Kong, D., Zhu, X., Ouyang, Z., 2021. China's Mars exploration mission and science investigation. Space Sci. Rev. 217 (4), 57.

Liu, Y., Wu, X., Zhao, Y.-Y.S., Pan, L., Wang, C., Liu, J., Zhao, Z., Zhou, X., Zhang, C., Wu, Y., Wan, W., Zou, Y., 2022. Zhurong reveals recent aqueous activities in Utopia Planitia, Mars. Sci. Adv. 8 (19), eabn8555.

McEwen, A.S., Eliason, E.M., Bergstrom, J.W., Bridges, N.T., Hansen, C.J., Delamere, W.A., Grant, J.A., Gulick, V.C., Herkenhoff, K.E., Keszthelyi, L., 2007. Mars reconnaissance orbiter's high resolution imaging science experiment (HiRISE). J. Geophys. Res. 112 (E5), E05S02.

Michael, G.G., Neukum, G., 2010. Planetary surface dating from crater size–frequency distribution measurements: partial resurfacing events and statistical age uncertainty. Earth Planet. Sci. Lett. 294 (3), 223–229.

Nagle-McNaughton, T., Scuderi, L., 2021. Multistage evolution in Transverse Aeolian Ridges. Remote Sens. 13 (7), 1329.

Palucis, M.C., Jasper, J., Garczynski, B., Dietrich, W.E., 2020. Quantitative assessment of uncertainties in modeled crater retention ages on Mars. Icarus 341, 113623.

Reiss, D., van Gasselt, S., Neukum, G., Jaumann, R., 2004. Absolute dune ages and implications for the time of formation of gullies in Nirgal Vallis, Mars. J. Geophys. Res., Planets 109 (E6).

Rubanenko, L., Powell, T.M., Williams, J.-P., Daubar, I., Edgett, K.S., Paige, D.A., 2021. Challenges in crater chronology on Mars as reflected in Jezero crater. In: Soare, R.J., Conway, S.J., Williams, J.-P., Oehler, D.Z. (Eds.), Mars Geological Enigmas. Elsevier, pp. 97–122.

Ruff, S.W., Christensen, P.R., 2002. Bright and dark regions on Mars: particle size and mineralogical characteristics based on thermal emission spectrometer data. J. Geophys. Res. 107 (E12), 5127.

Silvestro, S., Vaz, D.A., Yizhaq, H., Esposito, F., 2016. Dune-like dynamic of Martian aeolian large ripples. Geophys. Res. Lett. 43 (16), 8384–8389.

Silvestro, S., Chojnacki, M., Vaz, D.A., Cardinale, M., Yizhaq, H., Esposito, F., 2020. Megaripple migration on Mars. J. Geophys. Res., Planets 125 (8), e2020JE006446.

Smith, D.E., Zuber, M.T., Frey, H.V., Garvin, J.B., Head, J.W., Muhleman, D.O., Pettengill, G.H., Phillips, R.J., Solomon, S.C., Zwally, H.J., Banerdt, W.B., Duxbury, T.C., Golombek, M.P., Lemoine, F.G., Neumann, G.A., Rowlands, D.D., Aharonson, O., Ford, P.G., Ivanov, A.B., Johnson, C.L., McGovern, P.J., Abshire, J.B., Afzal, R.S., Sun, X., 2001. Mars Orbiter Laser Altimeter: experiment summary after the first year of global mapping of Mars. J. Geophys. Res., Planets 106 (E10), 23689–23722.

Sullivan, R., Banfield, D., Bell, J.F., Calvin, W., Fike, D., Golombek, M., Greeley, R., Grotzinger, J., Herkenhoff, K., Jerolmack, D., Malin, M., Ming, D., Soderblom, L.A., Squyres, S.W., Thompson, S., Watters, W.A., Weitz, C.M., Yen, A., 2005. Aeolian processes at the mars Exploration Rover Meridiani Planum landing site. Nature 436 (7047), 58–61.

Sullivan, R., Arvidson, R., Bell III, J.F., Gellert, R., Golombek, M., Greeley, R., Herkenhoff, K., Johnson, J., Thompson, S., Whelley, P., Wray, J., 2008. Wind-driven particle mobility on Mars: insights from Mars Exploration Rover observations at "El Dorado" and surroundings at Gusev Crater. J. Geophys. Res., Planets 113 (E6).

Sullivan, R., Bridges, N., Herkenhoff, K., Hamilton, V., Rubin, D., 2014. Transverse aeolian ridges (TARs) as megaripples: rover encounters at Meridiani Planum, Gusev, and Gale. In: Eighth International Conference on Mars, p. 1424.

Vaz, D.A., Silvestro, S., Sarmento, P.T.K., Cardinale, M., 2017. Migrating meter-scale bedforms on Martian dark dunes: are terrestrial aeolian ripples good analogues? Aeolian Res. 26, 101–116.

Wilson, S.A., Zimbelman, J.R., 2004. Latitude-dependent nature and physical characteristics of transverse aeolian ridges on Mars. J. Geophys. Res., Planets 109 (E10).

Zhao, J., Xiao, Z., Huang, J., Head III, J.W., Wang, J., Shi, Y., Wu, B., Wang, L., 2021. Geological characteristics and targets of high scientific interest in the Zhurong landing region on Mars. Geophys. Res. Lett. 48 (20), e2021GL094903.

Zimbelman, J.R., 2010. Transverse aeolian ridges on Mars: first results from HiRISE images. Geomorphology 121 (1), 22–29.

Zimbelman, J.R., Williams, S.H., Johnston, A.K., 2012. Cross-sectional profiles of sand ripples, megaripples, and dunes: a method for discriminating between formational mechanisms. Earth Surf. Process. Landf. 37 (10), 1120–1125.

Zimbelman, J.R., Scheidt, S.P., 2014. Precision topography of a reversing sand dune at Bruneau Dunes, Idaho, as an analog for transverse aeolian ridges on Mars. Icarus 230, 29–37.

Zimbelman, J.R., Foroutan, M., 2020. Dingo gap: Curiosity went up a small transverse aeolian ridge and came down a megaripple. J. Geophys. Res., Planets 125 (12), e2020JE006489.